Research Square

Preprints are preliminary reports that have not undergone peer review.
They should not be considered conclusive, used to inform clinical practice,
or referenced by the media as validated information.

Theory of spin-polarized scanning tunneling microscopy with topological insulator tips

Lunhui Hu

lunhui@zju.edu.cn

Zhejiang University https://orcid.org/0000-0002-0376-3367

Zhuo-Yuan Shi

Zhejiang University

Chuang Li

Huazhong University of Science and Technology https://orcid.org/0000-0003-1895-1771

Lin Jiao

Zhejiang University https://orcid.org/0000-0002-8343-0190

Huiqiu Yuan

Zhejiang University https://orcid.org/0000-0002-9787-4884

Zhenyu Wang

University of Science and Technology of China https://orcid.org/0000-0002-4857-7234

Xianhui Chen

University of Science and Technology of China https://orcid.org/0000-0001-6947-1407

Article

Keywords:

Posted Date: November 27th, 2026

DOI: https://doi.org/10.21203/rs.3.rs-11784264/v1

License: This work is licensed under a Creative Commons Attribution 4.0 International License.
Read Full License

Additional Declarations: There is **NO** Competing Interest.

Theory of spin-polarized scanning tunneling microscopy with topological insulator tips

Zhuo-Yuan Shi,[1] Chuang Li,[1,*] Lin Jiao,[1,†] Huiqiu Yuan,[1] Zhenyu Wang,[2,3] Xianhui Chen,[2,3] and Lun-Hui Hu[1,‡]

[1] *Center for Correlated Matter and School of Physics, Zhejiang University, Hangzhou 310058, China*
[2] *Department of Physics, University of Science and Technology of China, Hefei, Anhui, China*
[3] *Hefei National Laboratory, University of Science and Technology of China, Hefei, 230088, China*

(Dated: November 19, 2026)

Topological insulators have enabled a new class of spin-sensitive scanning tunneling microscopy (STM) probes based on helical boundary states [1–3]. However, how these probes generate a net spin-polarized tunneling current remains unclear. We present a theory of spin-polarized STM with topological insulator tips and show that asymmetric tunneling-contact geometry and spin dephasing enable helical boundary states to generate a spin-polarized tunneling current. Within the standard Landauer-Büttiker formalism, we demonstrate this mechanism for a quantum spin Hall (QSH) insulator tip: asymmetric contacts make the two counter-propagating helical edge states, which carry opposite spins, traverse path lengths that differ by ΔL, and spin dephasing induces backscattering that reduces the conductance more strongly for the longer path. For a representative asymmetric contact and weak spin dephasing, the QSH tip exhibits a tunneling spin polarization of $P_s = -17.2\%$ under positive bias, whose magnitude can reach 50% for larger ΔL, and which remains robust against Rashba spin-orbit coupling. Crucially, this polarization, dominated by helical edge transport rather than by bulk states, naturally reverses sign with the bias polarity owing to spin-momentum locking. Our findings are consistent with recent STM experiments using topological tips.

I. INTRODUCTION

Topological quantum materials have opened new opportunities for quantum transport and device applications owing to their nontrivial band topology and low-dissipation transport properties [4–11]. Recent high-throughput computations have identified thousands of topological materials, which are now catalogued in open databases [12–14]. However, realizing direct functional applications typically requires the boundary-state transport to dominate at the Fermi level, though a fully gapped bulk is not strictly necessary. Among this broad family, topological insulators naturally satisfy this criterion, combining an insulating bulk with gapless boundary states that are protected by time-reversal symmetry [15–22]. Spin–momentum locking converts a charge current in these topological boundary states into a net spin polarization, and the robustness of these states against nonmagnetic disorder makes this spin-sensitive transport highly attractive for promising low-dissipation spintronic devices [23–27]. In addition to their considerable device potential, helical boundary states of topological insulators have recently afforded an unexpected and distinct application: spin-sensitive probes of quantum matter [1–3].

A striking realization of this probe concept is scanning tunneling microscopy (STM) using topological-insulator tips [1–3]. In this approach, spin-selective tunneling originates from spin-momentum-locked helical boundary states within the tip itself. The first demonstration employed SmB_6 nanowires, a candidate topological Kondo insulator [28–32], as STM tips to image the bicollinear antiferromagnetic order of $Fe_{1.03}Te$ with atomic resolution at 4 K [1]. The magnetic contrast vanished upon warming above ~ 10 K, concomitant with the suppression of the topological surface states in the SmB_6 tip [1, 33], well below the Néel temperature (~ 50 K) of $Fe_{1.03}Te$. Crucially, reversing the STM bias polarity produced a π phase reversal of the magnetic stripes, showing that the spin selectivity of the tip can be reversed purely electrically.

More recently, another topological insulator, Bi_4Br_4 [34–38], with helical boundary states, has also been used as an STM tip to image spin-resolved quasiparticle interference (QPI) in the d-wave layered altermagnet KV_2Se_2O [2]. Strikingly, reversing the STM bias rotates the dominant QPI pattern by 90°. In a d-wave altermagnet, the spin splitting changes sign under such a rotation because of the $[C_2||C_4]$ symmetry [39–42]; the observed rotation thus directly indicates that the spin selectivity of the Bi_4Br_4 tip reverses sign with bias polarity. The same bias-driven reversal of spin-selective QPI on KV_2Se_2O has also been independently observed with SmB_6 tips [3]. Meanwhile, conventional spin-polarized STM using ferromagnetic Cr tips has observed QPI patterns with the same 90° rotation on KV_2Se_2O and its sister compound RbV_2Se_2O, albeit with the contrast switched by an applied magnetic field rather than by the bias [43, 44]. This underscores the distinctive capability of topological tips to achieve comparable spin selectivity through bias reversal alone, without tip magnetization. Nevertheless, the microscopic mechanism by which helical boundary states generate a spin-polarized tunneling current remains unclear.

Since a topological-insulator tip preserves time-reversal symmetry, resolving this puzzle requires a theoretical framework distinct from that of conventional ferromagnetic tips, whose spin selectivity mainly originates from unequal spin-resolved densities of states [45–49]. Specifically, in such a tip, the two counter-propagating helical

* lichuang.zju@outlook.com
† lin.jiao@zju.edu.cn
‡ lunhui@zju.edu.cn

modes of opposite spin give exactly balanced spin-resolved densities of states [Fig. 1(a)]. The ferromagnetic-tip framework therefore predicts vanishing spin selectivity and cannot explain the observed bias-reversal effect. Importantly, because an STM tip terminates in a sharp apex, the two helical boundary states couple to the sample at different distances, making the tunneling-contact geometry asymmetric [see Fig. 1]. To model this transport, we employ a nonequilibrium Landauer-Büttiker formalism with current-conserving Büttiker probes [50–54] that treat spin dephasing as spin-relaxing backscattering [Fig. 1(a)].

Our central finding is that a net spin-polarized tunneling current from topological-insulator tips arises only when the asymmetric contact geometry and spin dephasing coexist and act together. First, the tip-apex-induced asymmetric tunneling-contact geometry (without spin dephasing) creates helical propagation paths whose lengths differ by ΔL, but does not induce backscattering of the edge modes, leaving the spin-resolved transmissions balanced [Fig. 1(b)]. Second, with spin dephasing but symmetric propagation paths, both helical channels experience identical suppression, so the spin-resolved transmissions remain balanced [Fig. 1(c)]. Only when the two act together do the helical channels acquire unequal transmission probabilities and thus a net tunneling spin polarization ($P_s \neq 0$) [Fig. 1(d)]. Moreover, the finite P_s is dominated by helical edge transport, reverses sign with the bias polarity owing to spin-momentum locking, and can be substantially enhanced by increasing ΔL. As a concrete demonstration, we employ a quantum spin Hall (QSH) insulator tip to quantify the resulting spin polarization, obtaining $P_s \approx -17.2\%$; these results are qualitatively consistent with recent experiments on topological STM probes [1–3] and provide design principles for optimizing the spin sensitivity of such probes.

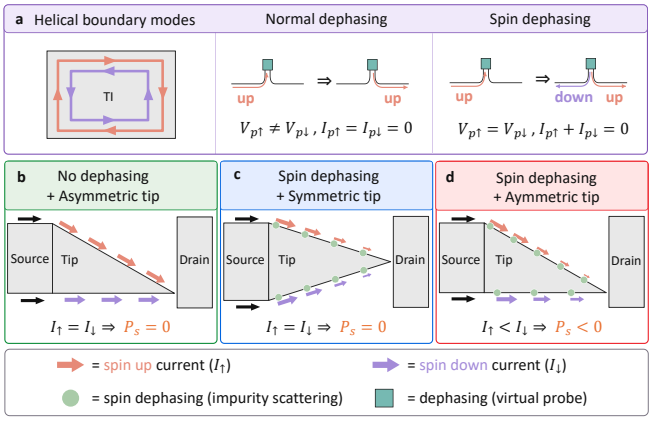

FIG. 1. Mechanism of spin-selective tunneling in topological-insulator tips. (a) Comparison of normal and spin dephasing in helical boundary modes with opposite spins. Normal (spin-conserving) dephasing produces no backscattering of the edge states, whereas spin-relaxing dephasing induces spin-flip backscattering. (b)–(d) Three main cases illustrating the requirements for tunneling spin polarization: (b) asymmetric geometry without dephasing (or with normal dephasing only), yielding unequal path lengths but balanced transmissions; (c) symmetric geometry with spin dephasing, where both channels are equally suppressed; and (d) the combination of asymmetric geometry and spin dephasing, where unequal spin-flip scattering generates a finite spin-polarized current.

II. SPIN-RESOLVED LANDAUER-BÜTTIKER FORMALISM

The standard theory of STM is built on Bardeen's transfer-Hamiltonian formalism, which treats electron tunneling perturbatively to leading order in the tip-sample coupling [55–58]. In its application to spin-polarized STM with ferromagnetic tips, the tunneling matrix element is taken to be spin independent, and the spin-resolved current is given by $I_\sigma(U) \propto \int dE\, |M|^2\, \rho_{t,\sigma}(E - eU)\, \rho_{s,\sigma}(E)\, \big[f(E-eU) - f(E)\big]$, where $\sigma = \uparrow, \downarrow$ labels the spin of the tunneling electron, U is the bias voltage applied between the tip and the sample, M is the tunneling matrix element, $\rho_{t,\sigma}(E)$ and $\rho_{s,\sigma}(E)$ are the spin-resolved densities of states of the tip and the sample, respectively, and $f(E) = [e^{E/(k_B T)} + 1]^{-1}$ is the Fermi distribution function. Within this description, the spin polarization of the tunneling current, $P_s = (I_\uparrow - I_\downarrow)/(I_\uparrow + I_\downarrow)$, originates entirely from the imbalance between $\rho_{t,\uparrow}$ and $\rho_{t,\downarrow}$ [45–49]. This perturbative picture, however, is inadequate for a topological-insulator tip [59]: the spin signal is carried by helical boundary states that propagate along the tip before tunneling, and their transmission is shaped by repeated scattering within the tip and by spin dephasing along the edge paths [see Fig. 1], effects that a leading-order tunneling matrix element cannot capture [60–62]. We therefore employ the Landauer-Büttiker formalism within the nonequilibrium Green-function approach, which describes transport as phase-coherent transmission between reservoirs and incorporates dephasing through current-conserving Büttiker probes [50–54].

As illustrated in Fig. 1(d), we consider transport from the topological-insulator tip (the left lead L), through the central scattering region, to the sample (the right lead R). To implement dephasing, we attach Büttiker probes to N selected lattice sites of the topological-insulator tip. At each selected site p, the probe modifies the tip Hamiltonian by adding a self-energy,

$$\Sigma^r_{p\sigma} = -i\beta\Pi_{p\sigma}/2, \tag{1}$$

where $\Pi_{p\sigma}$ projects onto all orbitals of spin σ at site p (i.e., the spin-σ block of the on-site Hilbert space), and $\beta \geq 0$ is the spin-independent probe (dephasing) strength. We consider two types of dephasing mechanisms [52]: (i) normal dephasing (spin-conserving) imposes $I_{p\uparrow} = I_{p\downarrow} = 0$ so that generally $V_{p\uparrow} \neq V_{p\downarrow}$, and (ii) spin dephasing (spin-relaxing) imposes $V_{p\uparrow} = V_{p\downarrow}$ and $I_{p\uparrow} + I_{p\downarrow} = 0$. Here $V_{p\sigma}$ and $I_{p\sigma}$ denote the voltage and current of the corresponding Büttiker probe.

To determine the spin selectivity of the topological-insulator tip, we model the sample as a spin-degenerate

metal without spin-orbit coupling, so that any spin polarization of the current can be attributed solely to the tip. All terminals, including the Büttiker probes, are then treated on an equal footing within the multiterminal Landauer-Büttiker formalism. The transmission from terminal j to terminal i is given by the Caroli formula [63],

$$T_{i\leftarrow j}(E) = \mathrm{Tr}[\Gamma_i G^r(E)\Gamma_j G^a(E)], \tag{2}$$

where E is the electron energy, $G^{r/a}(E)$ are the retarded/advanced Green functions of the central region dressed by the self-energies of the physical leads (L, R) and the local Büttiker probes ($p = 1, 2, \cdots, N$), and $\Gamma_i = i(\Sigma_i^r - \Sigma_i^a)$ is the broadening matrix [64]. Here $i = (\alpha, \sigma)$ and $j = (\alpha', \sigma')$ are composite terminal-spin indices, with $\alpha, \alpha' \in \{L, R, 1, 2, \ldots, N\}$ and $\sigma, \sigma' = \{\uparrow, \downarrow\}$. The trace runs over all central-region spatial and orbital degrees of freedom. As a result, the probe voltages $V_{p\sigma}$ are determined self-consistently from the spin-resolved multiterminal Landauer-Büttiker equations [53],

$$I_i = \frac{e^2}{h}\sum_{j\neq i}(T_{i\leftarrow j}V_j - T_{j\leftarrow i}V_i), \tag{3}$$

where I_i is the current entering terminal i: the first term collects electrons injected from j into i, and the second collects electrons leaving i towards j. At zero temperature we set $V_{L\sigma} = V$ and $V_{R\sigma} = 0$, with V the applied STM bias. Within linear response, the current collected by the right lead is $I_{R\sigma}(E) = (e^2/h)T^{\mathrm{eff}}_{R\sigma\leftarrow L}(E)V$, with the effective spin-resolved transmission

$$T^{\mathrm{eff}}_{R\sigma\leftarrow L}(E) = \sum_{\sigma'}\left[T_{R\sigma\leftarrow L\sigma'} + \sum_p T_{R\sigma\leftarrow p\sigma'}\frac{V_{p\sigma'}}{V}\right]. \tag{4}$$

Eq. (4) is the central quantity of our theory. Its first term, the Bardeen-type term, collects all direct tunneling processes from the tip to the sample. Its second term, the Büttiker-probe-mediated term, collects the indirect processes in which an electron is absorbed by a Büttiker probe, reinjected at the probe voltage $V_{p\sigma'}$ with or without spin flip according to the dephasing condition, and subsequently transmitted to the sample. The spin polarization of the tunneling current [65] is then given by

$$P_s(E) = \frac{T^{\mathrm{eff}}_{R\uparrow\leftarrow L}(E) - T^{\mathrm{eff}}_{R\downarrow\leftarrow L}(E)}{T^{\mathrm{eff}}_{R\uparrow\leftarrow L}(E) + T^{\mathrm{eff}}_{R\downarrow\leftarrow L}(E)}. \tag{5}$$

Reversing the bias polarity amounts to interchanging $L \leftrightarrow R$ in Eq. (4). While $P_s(E)$ defined in Eq. (5) characterizes the injection from the tip to the sample ($L \to R$), reversing the bias corresponds to the reverse injection process ($R \to L$), which we denote as $\bar{P}_s(E)$. Owing to the spin-momentum locking of the helical modes, reversing the transport direction reverses the spin orientation carried by the edge modes. Consequently, we expect the tunneling spin polarization to reverse its sign upon reversing the bias polarity, i.e.,

$$\mathrm{sign}\big[P_s(E)\bar{P}_s(E)\big] < 0. \tag{6}$$

This distinctive prediction is confirmed by the calculations presented in Sec. IV, and further details are provided in the Supplemental Material (SM) [66].

Before model calculations, we make a qualitative comparison between ferromagnetic and topological-insulator tips. In a ferromagnetic tip, the Büttiker probes are absent, so Eq. (4) reduces to $T^{\mathrm{eff}}_{R\sigma\leftarrow L} = T_{R\sigma\leftarrow L} \propto \rho_{t,\sigma}$, where $\rho_{t,\sigma}$ is the spin-resolved density of states of the tip. In a topological-insulator tip, the Büttiker probe-mediated second term in Eq. (4) drives the spin selectivity: spin dephasing redistributes the two spin populations, which, combined with the asymmetric edge paths, yields unequal effective transmissions and a finite polarization.

III. MODEL AND NUMERICAL RESULTS

The general formalism of Sec. II identifies the conditions under which a topological-insulator tip can generate a spin-polarized current, but it cannot by itself answer three quantitative questions: how large the polarization is, how it depends on the contact geometry and the dephasing strength, and whether it is indeed carried by helical edge transport within the bulk gap rather than by bulk states. To address these questions, we construct in this section a minimal lattice model of a topological-insulator tip with an asymmetric tunneling contact and a controlled placement of the Büttiker probes, and compute the tunneling spin polarization P_s as a function of the edge-path difference ΔL and the dephasing strength β. As the minimal model hosting counter-propagating helical boundary states, we employ a quantum spin Hall (QSH) insulator tip [2].

A. QSH tip Hamiltonian and contact geometry

For concreteness, we model the QSH tip and the normal-metal sample on a square lattice with lattice constant $a = 1$. At each site $\boldsymbol{r} = (x, y)$, $c_{\boldsymbol{r}}$ is the four-component electron annihilation operator in the basis $\{|s,\uparrow\rangle, |p_-,\uparrow\rangle, |s,\downarrow\rangle, |p_+,\downarrow\rangle\}$. The Pauli matrices σ_i and τ_i ($i = x, y, z$) act on spin and orbital spaces, respectively, while σ_0 and τ_0 denote the identity matrices. The real-space BHZ Hamiltonian reads [16],

$$H_{\mathrm{QSH}} = \sum_{\boldsymbol{r}} c^\dagger_{\boldsymbol{r}} h_0 c_{\boldsymbol{r}} + \sum_{\boldsymbol{r},\hat{\mu}=x,y}\left(c^\dagger_{\boldsymbol{r}+\hat{\mu}} T_{\hat{\mu}} c_{\boldsymbol{r}} + \mathrm{H.c.}\right), \tag{7}$$

where $h_0 = (M - 4t)\sigma_0\tau_z$ is the on-site term, and $T_x = t\sigma_0\tau_z - \frac{iA}{2}\sigma_z\tau_x$ and $T_y = t\sigma_0\tau_z - \frac{iA}{2}\sigma_0\tau_y$ are the nearest-neighbor hopping matrices along the x and y directions, respectively. Here, M controls the band inversion, t is the orbital-dependent hopping amplitude, and A sets the interorbital hopping strength. The QSH phase emerges when the mass term is inverted at the Γ point but not at the M point, which requires $0 < M < 4t$ (assuming $t > 0$). Moreover, the Hamiltonian preserves time-reversal

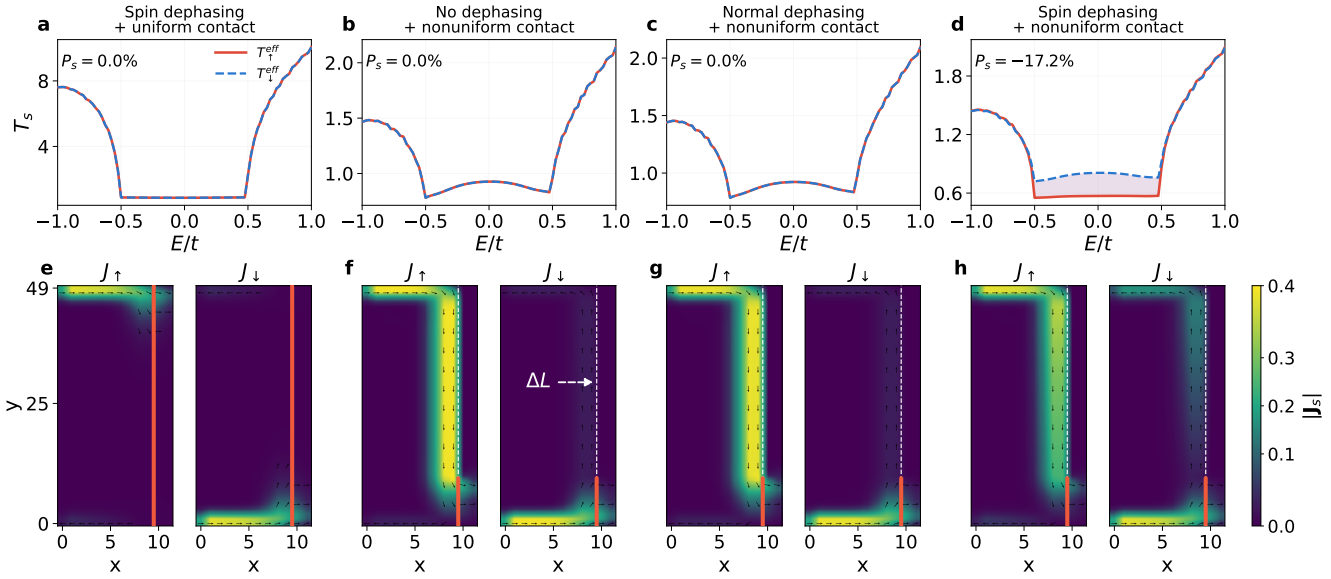

FIG. 2. Spin-resolved transport and local currents for different contact geometries and dephasing mechanisms. (a)–(d) Spin-resolved effective transmission spectra $T^{\mathrm{eff}}_{R\uparrow\leftarrow L}(E)$ (solid red) and $T^{\mathrm{eff}}_{R\downarrow\leftarrow L}(E)$ (dashed blue) for four configurations: (a) symmetric contact with spin dephasing, (b) asymmetric contact without dephasing, (c) asymmetric contact with normal dephasing, and (d) asymmetric contact with spin dephasing. Only the coexistence of an asymmetric geometry and spin dephasing (d) yields unequal spin-resolved transmissions within the bulk gap ($|E| < 0.5t$). (e)–(h) Real-space distributions of the spin-resolved local currents $J_\uparrow$ (left) and $J_\downarrow$ (right) at $E = 0.01t$, corresponding to the four conditions in (a)–(d), respectively. At the tip-sample interface, solid red lines denote active tunnel contacts, while dashed white lines denote regions without tunneling. Colors encode the magnitude $|J_s|$, and arrows (normalized for visibility) indicate the local current direction. An enhanced spin-flip return flow along the longer upper edge is visible in (h).

symmetry and conserves σ_z (i.e., $[H_{\mathrm{QSH}}, \sigma_z\tau_0] = 0$), so the two spin blocks decouple and the spin-resolved analysis below is unambiguous. Within the bulk gap $|E| < |M|$, the system hosts a single Kramers pair of helical edge states [see the SM [66]], which mediate the spin-selective transport studied in this work. The effect of Rashba spin-orbit coupling, which breaks the σ_z conservation, is discussed in Sec. VI.

The normal-metal sample contains two degenerate orbitals, with the electron annihilation operator $d_{\boldsymbol{r}} = (d_{\boldsymbol{r},1,\uparrow}, d_{\boldsymbol{r},2,\uparrow}, d_{\boldsymbol{r},1,\downarrow}, d_{\boldsymbol{r},2,\downarrow})^{\mathsf{T}}$. The Hamiltonian reads

$$H_{\mathrm{NM}} = \epsilon_m \sum_{\boldsymbol{r}} d^\dagger_{\boldsymbol{r}} d_{\boldsymbol{r}} - t_m \sum_{\boldsymbol{r},\hat{\mu}=x,y} \left(d^\dagger_{\boldsymbol{r}+\hat{\mu}} d_{\boldsymbol{r}} + \mathrm{H.c.} \right), \quad (8)$$

where $\epsilon_m = 4t_m - \mu_m$ is the on-site energy, μ_m is the chemical potential, and t_m is the nearest-neighbor hopping amplitude. The system is semi-infinite along the x direction and has a width of N_y sites along the y direction. For the transport calculation, we retain a finite central region comprising a tip segment ($0 \le x \le L_{\mathrm{QSH}}$) and a sample segment ($L_{\mathrm{QSH}}+1 \le x \le L_{\mathrm{QSH}}+L_{\mathrm{NM}}$), while the remaining semi-infinite portions are incorporated through the self-energies in Eq. (2). The tip-sample coupling at the interface $x = L_{\mathrm{QSH}}$ is given by

$$H_{\mathrm{contact}} = -t_c \sum_{y\in\mathcal{W}_c} \left(d^\dagger_{L_{\mathrm{QSH}}+1,y} c_{L_{\mathrm{QSH}},y} + \mathrm{H.c.} \right), \quad (9)$$

where t_c is the coupling constant, and the set $\mathcal{W}_c$ specifies the contacted sites. Specifically, (i) a symmetric (uniform) contact corresponds to $\mathcal{W}_c = \{0, \ldots, N_y - 1\}$, whereas (ii) an asymmetric (nonuniform) contact is defined by $\mathcal{W}_c = \{0, \ldots, N_c - 1\}$ with $1 \le N_c \le N_y - 1$. The asymmetric contact captures the finite size and sharp apex of an STM tip, so that the two helical edge states travel different effective distances before reaching the sample. This path asymmetry is quantified by

$$\Delta L = N_y - N_c. \quad (10)$$

To further incorporate dephasing along the helical edge propagation paths, we attach local Büttiker probes to the outermost three lattice layers along the upper, lower, and right boundaries of the QSH segment within the central region, with the dephasing strength quantified by the parameter β. Finally, we apply Eq. (4) and Eq. (5) to compute the effective transmissions and the tunneling spin polarization, respectively. The model parameters are set to $M = 0.5$, $t = 1$, $A = 1$, $t_m = 1$, $\mu_m = 2$, and $t_c = 0.6$.

B. Spin-resolved transmission spectra

Figure 2(a)–(d) display the calculated spin-resolved effective transmission spectra $T^{\mathrm{eff}}_{R\uparrow\leftarrow L}(E)$ and $T^{\mathrm{eff}}_{R\downarrow\leftarrow L}(E)$ for four distinct configurations. Inside the bulk gap

($|E| < 0.5$), transport is governed by the helical edge modes. A key observation is that neither the contact asymmetry nor the dephasing mechanism alone yields appreciable spin selectivity. For a symmetric contact ($\Delta L = 0$), spin dephasing suppresses both helical channels identically, preserving a vanishing polarization [Fig. 2(a)]. Similarly, when $\Delta L \neq 0$, an asymmetric contact either without dephasing [Fig. 2(b)] or with normal dephasing [Fig. 2(c)] leaves the two spin-resolved transmissions strictly degenerate across the bulk gap.

In stark contrast, the interplay between contact asymmetry and spin-relaxing dephasing lifts this degeneracy [Fig. 2(d)]. For $\Delta L = 40$ and $\beta = 0.03$, the effective transmission for spin-up is significantly reduced relative to spin-down, yielding a net spin polarization of $P_s = -17.2\%$ at $E = 0.01$. The negative sign of P_s is a direct consequence of the specific chirality (spin-momentum locking) of the helical edge modes in our model. The spin-up and spin-down electrons form clockwise and counterclockwise propagating modes along the boundaries. Since the asymmetric contact makes the shorter lower edge more transmissive, the net spin polarization is dominated by the spin-down electrons propagating along this edge towards the contact, yielding $P_s < 0$.

To explicitly verify this microscopic origin, we reverse the chirality of the edge states by flipping the sign of A solely in the y-direction hopping T_y (i.e., $A \to -A$ while keeping T_x unchanged) in Eq. (7). This operation swaps the propagation directions of the spin-up and spin-down modes. Under the identical asymmetric contact geometry and spin-relaxing dephasing, this chirality reversal exactly flips the dominant spin species, resulting in a positive tunneling spin polarization of $P_s = +17.2\%$ [see the SM [66]]. Therefore, these results establish that both contact asymmetry and spin relaxation are essential prerequisites for spin-selective tunneling from a QSH tip, with the sign of P_s serving as a direct fingerprint of its spin-momentum locking orientation.

C. Spatial distributions of spin-resolved currents

To further elucidate the real-space mechanism underlying this spin-selective transport, we examine the spatial distributions of the spin-resolved local currents at $E = 0.01$, as shown in Figs. 2(e)–(h). For a symmetric contact ($\Delta L = 0$) with spin dephasing, both helical edge pathways are geometrically equivalent, so their spin-relaxing attenuations remain strictly balanced, yielding equal spin-up and spin-down currents [Fig. 2(e)]. For an asymmetric contact ($\Delta L \neq 0$) in the absence of spin dephasing or with normal dephasing, elastic propagation along the extended upper edge is lossless, and spin remains locked to momentum all the way to the sample. The two helical channels therefore contribute equal spin-resolved currents, preserving a vanishing net polarization [Figs. 2(f) and 2(g)]. A pronounced asymmetry emerges exclusively when spin-relaxing dephasing coexists with the asymmetric contact [Fig. 2(h)]. Along the geometrically extended upper edge, electrons undergo a longer propagation distance, thereby accumulating stronger spin-flip backscattering. This unequal spin-flip scattering leads to unequal spin-resolved transmissions reaching the sample, consistent with the calculated tunneling spin polarization.

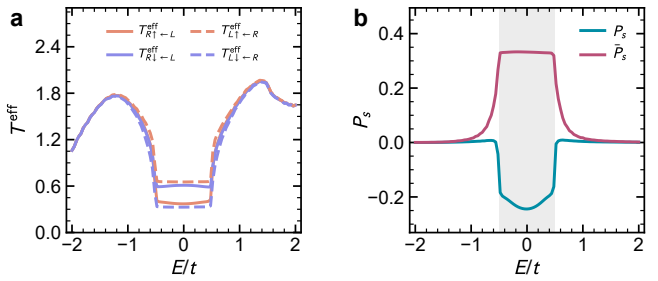

FIG. 3. Bias-polarity-induced reversal of tunneling spin polarization. (a) Spin-resolved effective transmissions $T^{\rm eff}_{R\uparrow\leftarrow L}(E)$ (orange) and $T^{\rm eff}_{R\downarrow\leftarrow L}(E)$ (blue) for tip-to-sample (solid) and sample-to-tip (dashed) transport. (b) The corresponding tunneling spin polarization P_s for tip-to-sample ($P_s < 0$, red) and sample-to-tip ($P_s > 0$, blue). Reversing the bias polarity reverses the sign of P_s.

Further details, including the local current calculations, the parameter dependence of P_s (ΔL and β), and its weak sensitivity to the contact hopping t_c [see Eq. (9)], are provided in the SM [66].

IV. BIAS-POLARITY-INDUCED REVERSAL OF SPIN SELECTIVITY

As discussed above, Eq. (6) captures a unique property of topological-insulator tips that is absent in conventional ferromagnetic tips: the sign reversal of spin selectivity with bias polarity. To confirm this distinctive prediction, we now examine the bias dependence of the tunneling spin polarization P_s. As shown in Fig. 3, reversing the STM bias polarity reverses the sign of P_s. Owing to the geometric asymmetry and spin-relaxing dephasing, the shorter lower edge remains the more transmissive channel for both transport directions. However, because of the spin-momentum locking of the QSH edge states, reversing the propagation direction reverses the spin orientation carried by the electrons along each edge [Fig. 3(a)]. Consequently, the geometrically favored lower-edge path carries opposite spins under opposite biases, leading to a sign reversal of P_s, although its magnitude may differ due to the self-consistent probe potentials [Fig. 3(b)]. This bias-driven sign reversal is consistent with the spin-resolved STM experiments using topological insulator tips [1–3].

Crucially, our results show that this tunneling spin selectivity is predominantly carried by the helical edge states. As shown in Fig. 3(b), $|P_s|$ remains robust and finite as long as the electron energy E lies within the bulk gap ($|E| < 0.5$), where the gapless helical edge states

serve as the exclusive transport channels. Once E lies outside the bulk gap, topologically trivial bulk modes begin to participate in the tunneling process. Because these bulk modes are largely immune to the edge path asymmetry, they carry no net spin selectivity, thereby diluting the total tunneling spin polarization and causing $|P_s|$ to drop rapidly towards zero. This sharp contrast between the edge-dominated and bulk-participating regimes provides compelling evidence that the observed tunneling spin polarization originates fundamentally from the path-asymmetric helical edge transport.

This strong dependence of P_s on the topological boundary states is consistent with the SmB_6 tip experiment [1], where the spin contrast vanishes concomitantly with the suppression of the topological surface states above ~ 10 K, establishing topological electronic states as the essential prerequisite for the spin-selective tunneling. Furthermore, our transport framework could reproduce the magnetic stripe contrast and its bias-induced reversal observed in the experiment [see the SM [66]].

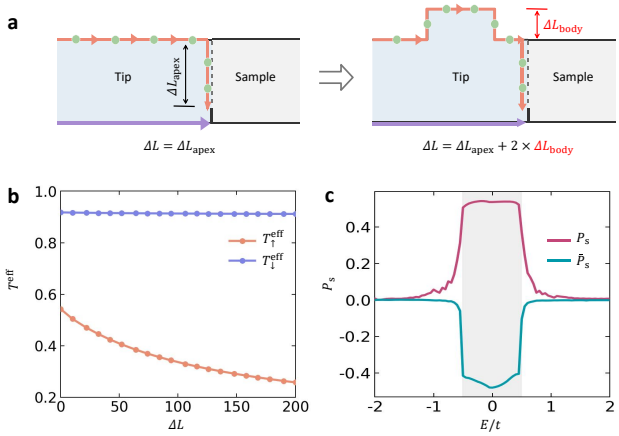

FIG. 4. Geometry-controlled enhancement of tunneling spin polarization. (a) Significant enlargement of the edge-path difference ΔL: arising solely from the tip apex (left) versus further extended by a geometric modification of the tip body (right). (b) Spin-up transmission decreases with increasing ΔL toward an Ohmic regime, while spin-down transmission along the clean lower edge remains quantized. (c) Tunneling spin polarization for positive (P_s) and negative ($\bar{P}_s$) bias polarities at $\Delta L = 100$, reaching $\sim 50\%$ in magnitude.

V. GEOMETRY-GUIDED TIP DESIGN

The contact asymmetry that drives the spin selectivity need not be limited to the atomic-scale tunneling apex: the tip body itself provides a practical knob for controlling helical edge transport. Because the spin-flip backscattering accumulated by a helical mode grows with its propagation distance, we can establish a simple design principle to selectively attenuate one helical edge channel by extending its length, while leaving the other channel intact. As illustrated in Figs. 4(a), we geometrically extend the upper edge of the tip body, such that the total edge-path difference ΔL now combines this macroscopic contribution with the atomic-scale apex asymmetry. Spin-relaxing dephasing centers act along the extended upper edge, whereas the shorter lower edge remains clean. With increasing ΔL, the spin-up transmission along the extended edge is progressively suppressed. In stark contrast, the spin-down transmission along the clean lower edge remains close to its quantized value, characteristic of ballistic helical edge transport [Fig. 4(b)]. The resulting imbalance strongly amplifies the tunneling spin polarization, exceeding 50% under both positive and negative bias polarities [Fig. 4(c)].

This strategy bypasses the need for atomically precise engineering of the tunneling apex. Since some degree of spin relaxation is inevitable during edge propagation in realistic materials, the engineered path imbalance translates directly into strong spin selectivity, without microscopic control over the scatterer distribution. Macroscopic tip geometry thus emerges as an accessible and robust route to optimizing the spin sensitivity of topological STM probes.

VI. EFFECT OF SPIN-ORBIT COUPLING

In the preceding sections where spin-orbit coupling (SOC) is absent, the tunneling spin polarization $P_s(E)$ is strictly defined by Eq. (5) within the σ_z-conserving basis. However, realistic topological insulators may also host SOC, which breaks this conservation. To quantify this effect, we add a Rashba SOC term to the QSH tip,

$$H_R = i\frac{\alpha_R}{2}\sum_{\boldsymbol{r}}\left(c^\dagger_{\boldsymbol{r}+\hat{x}}\sigma_y\tau_0 c_{\boldsymbol{r}} - c^\dagger_{\boldsymbol{r}+\hat{y}}\sigma_x\tau_0 c_{\boldsymbol{r}}\right) + \text{H.c.}, \quad (11)$$

where α_R is the SOC strength. Here, we only consider spin-relaxing dephasing. With finite α_R, the composite terminal-spin indices used previously are no longer applicable. Instead, Eqs. (2) and (3) describe the total tunneling from terminal i to terminal j, where $i = \{L, R, 1, 2, \cdots, N\}$ now denotes only the physical lead or probe index, and the spin degree of freedom must be explicitly traced out within each terminal. Consequently, the total current collected by the right lead is $I_R(E) = (e^2/h)T^{\rm eff}_{R\leftarrow L}(E)V$ with $T^{\rm eff}_{R\leftarrow L}(E) = \mathrm{Tr}[\Gamma_R\mathcal{T}_R(E)]$, where we define the effective transmission matrix as

$$\mathcal{T}_R(E) = G^r(E)\left[\Gamma_L + \sum_p \Gamma_p\frac{V_p}{V}\right]G^a(E). \quad (12)$$

The probe voltages V_p are obtained by solving Eq. (3). To further extract the spin-resolved contributions from $T^{\rm eff}_{R\leftarrow L}(E)$, we define a reduced matrix by taking a partial trace over the spatial and orbital degrees of freedom within the central region:

$$\mathcal{S}(E) = \mathrm{Tr}'\left[\Gamma_R^{1/2}\mathcal{T}_R(E)\Gamma_R^{1/2}\right], \quad (13)$$

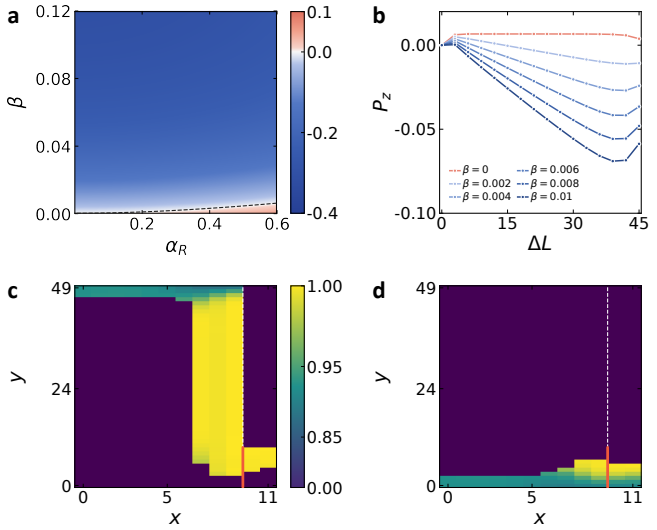

FIG. 5. Effect of Rashba SOC on tunneling spin polarization. (a) Tunneling spin polarization P_z in the α_R-β plane at $E = 0.01t$; the dashed contour marks $P_z = 0$. Spin dephasing dictates the dominant polarization, whereas Rashba SOC acts only as a weak competing mechanism. (b) P_z as a function of ΔL at $\alpha_R = 0.2$ for various β. (c,d) Real-space maps of the local spin polarization $P_z(\mathbf{r})$ for the (c) top and (d) bottom edge states at $\beta = 0$ [corresponding to the orange curve in (b)], isolating the pure SOC effect.

where Tr' traces over the spatial and orbital degrees of freedom while retaining the spin degrees of freedom. Consequently, $\mathcal{S}(E)$ is a 2×2 Hermitian matrix in spin space that encodes the full spin-resolved transmission properties of the system [67]. Thus, the tunneling spin polarization along the σ_i spin direction ($i = x, y, z$) is naturally defined as the normalized trace:

$$P_i(E) = \mathrm{Tr}[\sigma_i \mathcal{S}(E)]/\mathrm{Tr}[\mathcal{S}(E)]. \tag{14}$$

Here, the denominator $\mathrm{Tr}[\mathcal{S}(E)] = T^{\mathrm{eff}}_{R\leftarrow L}(E)$ represents the total transmission, while the numerator evaluates the spin-resolved transmission difference. In the SOC-free limit, the σ_z conservation ensures that $\mathcal{S}(E)$ is strictly diagonal in spin space (i.e., $\mathcal{S}_{\uparrow\downarrow} = \mathcal{S}_{\downarrow\uparrow} = 0$). Consequently, $P_z(E)$ exactly reduces to the original definition $P_s(E) = (\mathcal{S}_{\uparrow\uparrow} - \mathcal{S}_{\downarrow\downarrow})/(\mathcal{S}_{\uparrow\uparrow} + \mathcal{S}_{\downarrow\downarrow})$ given in Eq. (5).

We present the tunneling spin polarization $P_z(E)$ in Figs. 5(a) and (b) to discuss the role of SOC within our specific model. Figure 5(a) maps P_z in the α_R-β plane at $E = 0.01$. In the absence of SOC, the asymmetric tunneling-contact geometry ($\Delta L \neq 0$) and spin-relaxing dephasing ($\beta \neq 0$) yield a negative spin polarization [Fig. 2]. A finite Rashba SOC introduces a competing spin-mixing effect that drives P_z towards positive values; however, the dephasing-induced polarization remains dominant across the entire parameter range considered. Moreover, we investigate how ΔL modulates this competition in Fig. 5(b) for a fixed $\alpha_R = 0.2$. As the contact length decreases (i.e., as ΔL increases), spin-relaxing dephasing ($\beta \neq 0$) rapidly induces a net negative polarization, outweighing the weak positive polarization produced by pure SOC ($\beta = 0$). Crucially, both contributions vanish completely in the symmetric contact limit, confirming that geometric asymmetry is the essential prerequisite for finite spin polarization.

The positive polarization generated by pure SOC ($\beta = 0$) can be understood from the local spin-polarization maps in Figs. 5(c) and (d), with calculation details provided in the SM [66]. Because the horizontal (upper/lower) and vertical (right) edges have different crystalline orientations, the Rashba term induces an asymmetric spin rotation along the boundaries. For our QSH model, when reaching the contact, the electrons traversing the longer upper-edge path exhibit a stronger out-of-plane spin component compared to those on the shorter lower edge. The right-moving electrons along the bottom edge therefore lose more of their out-of-plane spin polarization, resulting in $I_\uparrow > I_\downarrow$ and thereby yielding a net positive P_z. While we focused on Rashba SOC in the BHZ model, exploring other SOC types or topological insulator models is left for future work.

VII. CONCLUSION AND DISCUSSIONS

In summary, we have developed a spin-resolved transport theory of scanning tunneling microscopy with topological-insulator tips. We bridge the Bardeen tunneling picture and the mesoscopic Landauer-Büttiker framework, establishing a unified Bardeen-Landauer-Büttiker picture for topological quantum probes. Our central finding is a cooperative mechanism for generating a net spin-polarized tunneling current: it requires the coexistence of an asymmetric tunneling-contact geometry (e.g., the tip apex) and spin-relaxing dephasing (e.g., magnetic impurities or spin-orbit scattering). While the geometric asymmetry creates helical edge paths of unequal lengths, the spin dephasing provides the necessary backscattering to break the balance between the counter-propagating channels. This joint effect produces unequal spin-resolved transmissions and a finite net polarization. Our predictions are qualitatively consistent with recent spin-selective STM experiments using SmB_6 and Bi_4Br_4 tips [1–3].

The resulting spin selectivity exhibits distinctive features that separate topological tips from conventional ferromagnetic tips. The polarization is strictly carried by the helical edge states within the bulk gap and naturally reverses its sign when the STM bias polarity is switched, directly reflecting the spin-momentum locking. Furthermore, this mechanism is robust against the spin-mixing effect induced by Rashba SOC. Notably, the polarization might be enhanced (exceeding 50%) by extending the macroscopic tip body, providing a practical route for geometry-guided probe design that bypasses the stringent requirement of atomic-scale apex engineering.

Our transport-based mechanism provides a route to bias-tunable spin selectivity without equilibrium tip mag-

netization, which is distinct from both electric-field-induced magnetoelectric responses [68] and interaction-induced surface magnetism [69, 70]. Looking forward, generalizing our work to other topological phases will offer new design principles for tunable spin-selective probes. In particular, layered topological materials such as $HfTe_5$ and $ZrTe_5$, which host helical boundary modes, represent promising candidates for realizing experimentally accessible topological probes [71–73].

Author contributions

L.-H. Hu and L. Jiao supervised the project. L.-H. Hu and C. Li conceived the project idea. Z.-Y. Shi and C. Li performed the calculations with help from L.-H. Hu. L.-H. Hu, Z.-Y. Shi and C. Li wrote the manuscript with input from L. Jiao, H.-Q. Yuan., Z.-Y. Wang and X.-H. Chen. All authors contributed to the scientific discussions and manuscript revisions.

Data availability

The datasets generated during this study are available from the corresponding authors upon request.

Code availability

The code used for transport calculation and data analysis is available from the corresponding authors upon request.

Funding

L.-H. Hu, L. Jiao and H.-Q. Yuan were supported by the National Key R&D Program of China (Grant Nos. 2025YFA1411500, 2022YFA1402200, 2023YFA1406100, and 2024YFA1207800), the National Natural Science Foundation of China (Grants Nos. 12374151, 12350710785, W2511006, 12561160109, 12574148), and the Zhejiang Provincial Natural Science Foundation of China (Grant No. LR25A040003). Z.-Y. Wang and X.-H. Chen were supported by the Quantum Science and Technology-National Science and Technology Major Project (Grant No. 2021ZD0302800), the HFNL Self-Deployed Project (ZB2025020200), the National Key R&D Program of the MOST of China (Grant No. 2022YFA1602600), the Scientific Research Innovation Capability Support Project for Young Faculty (Grant No. ZYGXQNJSKYCXNLZCXM-M25), and the National Natural Science Foundation of China (Grant No. 12488201).

Competing interests

The authors declare no competing interests.

Ethics declaration

Ethics declaration: not applicable.

[1] A. Aishwarya, Z. Cai, A. Raghavan, M. Romanelli, X. Wang, X. Li, G. D. Gu, M. Hirsbrunner, T. Hughes, F. Liu, L. Jiao, and V. Madhavan, Spin-selective tunneling from nanowires of the candidate topological kondo insulator SmB_6, Science **377**, 1218 (2022).

[2] Z. Wang, S. Yu, X. Cheng, X. Xiao, W. Ma, Y. Ma, F. Quan, H. Song, K. Zhang, Y. Zhang, W. Liu, P. Yadav, H. Sheng, A. Wang, X. Shi, Z. Wang, Q. Niu, Y. Gao, B. Xiang, J. Liu, Z. Wang, and X. Chen, Atomic-scale spin sensing of a two-dimensional *d*-wave altermagnet via helical tunneling, Nature 10.1038/s41586-026-11257-1 (2026).

[3] G. Yang, C. Li, C. Wang, X. Zhao, Y. Wan, H. Gui, G. Zeng, S. Cao, C. Hu, Q. Yu, Y. Zhang, D. Chen, Y. Liu, Y. Song, Y. Zhang, F. Liu, L.-H. Hu, L. Jiao, and H. Yuan, Visualizing spin-polarization of an altermagnet KV_2Se_2O via spin-selective tunneling, arXiv:2603.21969 (2026).

[4] M. Z. Hasan and C. L. Kane, Colloquium: Topological insulators, Reviews of Modern Physics **82**, 3045 (2010).

[5] X.-L. Qi and S.-C. Zhang, Topological insulators and superconductors, Reviews of Modern Physics **83**, 1057 (2011).

[6] C.-K. Chiu, J. C. Y. Teo, A. P. Schnyder, and S. Ryu, Classification of topological quantum matter with symmetries, Rev. Mod. Phys. **88**, 035005 (2016).

[7] A. Bansil, H. Lin, and T. Das, Colloquium: Topological band theory, Reviews of Modern Physics **88**, 021004 (2016).

[8] N. P. Armitage, E. J. Mele, and A. Vishwanath, Weyl and dirac semimetals in three-dimensional solids, Rev. Mod. Phys. **90**, 015001 (2018).

[9] B. Q. Lv, T. Qian, and H. Ding, Experimental perspective on three-dimensional topological semimetals, Rev. Mod. Phys. **93**, 025002 (2021).

[10] B. J. Wieder, B. Bradlyn, J. Cano, Z. Wang, M. G. Vergniory, L. Elcoro, A. A. Soluyanov, C. Felser, T. Neupert, N. Regnault, and B. A. Bernevig, Topological materials discovery from crystal symmetry, Nature Reviews Materials **7**, 196 (2022).

[11] C.-Z. Chang, C.-X. Liu, and A. H. MacDonald, Colloquium: Quantum anomalous hall effect, Reviews of Modern Physics **95**, 011002 (2023).

[12] T. Zhang, Y. Jiang, Z. Song, H. Huang, Y. He, Z. Fang, H. Weng, and C. Fang, Catalogue of topological electronic materials, Nature **566**, 475 (2019).

[13] F. Tang, H. C. Po, A. Vishwanath, and X. Wan, Comprehensive search for topological materials using symmetry indicators, Nature **566**, 486 (2019).

[14] M. G. Vergniory, L. Elcoro, C. Felser, N. Regnault, B. A. Bernevig, and Z. Wang, A complete catalogue of high-quality topological materials, Nature **566**, 480 (2019).

[15] C. L. Kane and E. J. Mele, Quantum spin Hall effect in graphene, Phys. Rev. Lett. **95**, 146802 (2005).

[16] B. A. Bernevig, T. L. Hughes, and S.-C. Zhang, Quantum spin hall effect and topological phase transition in hgte quantum wells, Science **314**, 1757 (2006).

[17] M. König, S. Wiedmann, C. Brüne, A. Roth, H. Buhmann, L. W. Molenkamp, X.-L. Qi, and S.-C. Zhang, Quantum spin hall insulator state in hgte quantum wells, Science **318**, 766 (2007).

[18] L. Fu, C. L. Kane, and E. J. Mele, Topological insulators

in three dimensions, Phys. Rev. Lett. **98**, 106803 (2007).
[19] D. Hsieh, D. Qian, L. Wray, Y. Xia, Y. S. Hor, R. J. Cava, and M. Z. Hasan, A topological Dirac insulator in a quantum spin Hall phase, Nature **452**, 970 (2008).
[20] H. Zhang, C.-X. Liu, X.-L. Qi, X. Dai, Z. Fang, and S.-C. Zhang, Topological insulators in Bi_2Se_3, Bi_2Te_3 and Sb_2Te_3 with a single Dirac cone on the surface, Nat. Phys. **5**, 438 (2009).
[21] Y. L. Chen, J. G. Analytis, J.-H. Chu, Z. K. Liu, S.-K. Mo, X. L. Qi, H. J. Zhang, D. H. Lu, X. Dai, Z. Fang, S. C. Zhang, I. R. Fisher, Z. Hussain, and Z.-X. Shen, Experimental realization of a three-dimensional topological insulator, Bi_2Te_3, Science **325**, 178 (2009).
[22] Y. Xia, D. Qian, D. Hsieh, L. Wray, A. Pal, H. Lin, A. Bansil, D. Grauer, Y. S. Hor, R. J. Cava, and M. Z. Hasan, Observation of a large-gap topological-insulator class with a single Dirac cone on the surface, Nat. Phys. **5**, 398 (2009).
[23] D. Pesin and A. H. MacDonald, Spintronics and pseudospintronics in graphene and topological insulators, Nat. Mater. **11**, 409 (2012).
[24] W. Han, Y. Otani, and S. Maekawa, Quantum materials for spin and charge conversion, npj Quantum Materials **3**, 27 (2018).
[25] Q. L. He, T. L. Hughes, N. P. Armitage, Y. Tokura, and K. L. Wang, Topological spintronics and magnetoelectronics, Nat. Mater. **21**, 15 (2022).
[26] O. Breunig and Y. Ando, Opportunities in topological insulator devices, Nat. Rev. Phys. **4**, 184 (2022).
[27] Y. Que, A. Kumar, and B. Weber, Two-Dimensional topological insulators: Promises, challenges, and future perspectives, Advanced Materials , e00030 (2026).
[28] M. Dzero, K. Sun, V. Galitski, and P. Coleman, Topological kondo insulators, Phys. Rev. Lett. **104**, 106408 (2010).
[29] N. Xu, P. K. Biswas, J. H. Dil, R. S. Dhaka, G. Landolt, S. Muff, C. E. Matt, X. Shi, N. C. Plumb, M. Radović, E. Pomjakushina, K. Conder, A. Amato, S. V. Borisenko, R. Yu, H.-M. Weng, Z. Fang, X. Dai, J. Mesot, H. Ding, and M. Shi, Direct observation of the spin texture in SmB_6 as evidence of the topological kondo insulator, Nature Communications **5**, 4566 (2014).
[30] M. Dzero, J. Xia, V. Galitski, and P. Coleman, Topological Kondo insulators, Annual Review of Condensed Matter Physics **7**, 249 (2016).
[31] L. Jiao, S. Rößler, D. Kasinathan, P. F. S. Rosa, C. Guo, H. Yuan, C.-X. Liu, Z. Fisk, F. Steglich, and S. Wirth, Magnetic and defect probes of the SmB_6 surface state, Science Advances **4**, eaau4886 (2018).
[32] L. Li, K. Sun, Ç. Kurdak, and J. W. Allen, Emergent mystery in the Kondo insulator samarium hexaboride, Nat. Rev. Phys. **2**, 463 (2020).
[33] M. Neupane, N. Alidoust, S.-Y. Xu, T. Kondo, Y. Ishida, D.-J. Kim, C. Liu, I. Belopolski, Y. J. Jo, T.-R. Chang, H.-T. Jeng, T. Durakiewicz, L. Balicas, H. Lin, A. Bansil, S. Shin, Z. Fisk, and M. Z. Hasan, Surface electronic structure of the topological Kondo-insulator candidate correlated electron system SmB_6, Nat. Commun. **4**, 2991 (2013).
[34] J.-J. Zhou, W. Feng, C.-C. Liu, S. Guan, and Y. Yao, Large-gap quantum spin Hall insulator in single layer bismuth monobromide Bi_4Br_4, Nano Lett. **14**, 4767 (2014).
[35] R. Noguchi, M. Kobayashi, Z. Jiang, K. Kuroda, T. Takahashi, Z. Xu, D. Lee, M. Hirayama, M. Ochi, T. Shirasawa, P. Zhang, C. Lin, C. Bareille, S. Sakuragi, H. Tanaka, S. Kunisada, K. Kurokawa, K. Yaji, A. Harasawa, V. Kandyba, A. Giampietri, A. Barinov, T. K. Kim, C. Cacho, M. Hashimoto, D. Lu, S. Shin, R. Arita, K. Lai, T. Sasagawa, and T. Kondo, Evidence for a higher-order topological insulator in a three-dimensional material built from van der Waals stacking of bismuth-halide chains, Nat. Mater. **20**, 473 (2021).
[36] N. Shumiya, M. S. Hossain, J.-X. Yin, Z. Wang, M. Litskevich, C. Yoon, Y. Li, Y. Yang, Y.-X. Jiang, G. Cheng, Y.-C. Lin, Q. Zhang, Z.-J. Cheng, T. A. Cochran, D. Multer, X. P. Yang, B. Casas, T.-R. Chang, T. Neupert, Z. Yuan, S. Jia, H. Lin, N. Yao, L. Balicas, F. Zhang, Y. Yao, and M. Z. Hasan, Evidence of a room-temperature quantum spin Hall edge state in a higher-order topological insulator, Nat. Mater. **21**, 1111 (2022).
[37] K.-S. Lin, G. Palumbo, Z. Guo, Y. Hwang, J. Blackburn, D. P. Shoemaker, F. Mahmood, Z. Wang, G. A. Fiete, B. J. Wieder, and B. Bradlyn, Spin-resolved topology and partial axion angles in three-dimensional insulators, Nat. Commun. **15**, 550 (2024).
[38] S. Yu, J. Deng, W. Liu, Y. Zhang, Y. Sun, N. Dhale, S. Li, W. Ma, Z. Wang, P. Wu, Z. Liang, X. Zhang, B. Lv, Z. Wang, Z. Wang, and X. Chen, Observation of robust one-dimensional edge channels in a three-dimensional quantum spin Hall insulator, Phys. Rev. X **14**, 041048 (2024).
[39] L. Šmejkal, J. Sinova, and T. Jungwirth, Emerging research landscape of altermagnetism, Phys. Rev. X **12**, 040501 (2022).
[40] L. Bai, W. Feng, S. Liu, L. Šmejkal, Y. Mokrousov, and Y. Yao, Altermagnetism: Exploring new frontiers in magnetism and spintronics, Adv. Funct. Mater. **34**, 2409327 (2024).
[41] S. S. Fender, O. Gonzalez, and D. K. Bediako, Altermagnetism: A chemical perspective, J. Am. Chem. Soc. **147**, 2257 (2025).
[42] T. Jungwirth, J. Sinova, R. M. Fernandes, Q. Liu, H. Watanabe, S. Murakami, S. Nakatsuji, and L. Šmejkal, Symmetry, microscopy and spectroscopy signatures of altermagnetism, Nature **649**, 837 (2026).
[43] J.-C. Gu, M. Hu, Z. Song, L. Wang, L. Wang, J. Zhang, J. Zhao, H. Li, S. Jin, X.-D. Zhang, G. Chen, H. Weng, Z. Wei, and T. Qian, Real-space identification of distinct magnetic configurations in a candidate *d*-wave altermagnet, arXiv:2606.29140 (2026).
[44] D. Mu, B. Jiang, Q. Duan, Z. Xu, X. Cheng, Y. Xiao, X. Han, X. Liang, Z. Luo, R. L. Kong, Q. Wang, J. Liu, J. Zhong, R. Zhong, Q. Gu, B. Lv, and H. Ding, Direct observation of quadruple spin-texture locking in a 2d *d*-wave altermagnet, arXiv:2604.18337 (2026).
[45] J. Tersoff and D. R. Hamann, Theory of the scanning tunneling microscope, Phys. Rev. Lett. **50**, 1998 (1983).
[46] R. Wiesendanger, H.-J. Güntherodt, G. Güntherodt, R. J. Gambino, and R. Ruf, Observation of vacuum tunneling of spin-polarized electrons with the scanning tunneling microscope, Phys. Rev. Lett. **65**, 247 (1990).
[47] M. Bode, Spin-polarized scanning tunnelling microscopy, Rep. Prog. Phys. **66**, 523 (2003).
[48] R. Wiesendanger, Spin mapping at the nanoscale and atomic scale, Reviews of Modern Physics **81**, 1495 (2009).
[49] H. Oka, O. O. Brovko, M. Corbetta, V. S. Stepanyuk, D. Sander, and J. Kirschner, Spin-polarized quantum confinement in nanostructures: Scanning tunneling mi-

croscopy, Rev. Mod. Phys. **86**, 1127 (2014).
[50] M. Büttiker, Four-terminal phase-coherent conductance, Physical Review Letters **57**, 1761 (1986).
[51] J. L. D'Amato and H. M. Pastawski, Conductance of a disordered linear chain including inelastic scattering events, Physical Review B **41**, 7411 (1990).
[52] H. Jiang, S. Cheng, Q.-f. Sun, and X. C. Xie, Topological insulator: A new quantized spin hall resistance robust to dephasing, Physical Review Letters **103**, 036803 (2009).
[53] A.-M. Guo and Q.-f. Sun, Spin-selective transport of electrons in DNA double helix, Physical Review Letters **108**, 218102 (2012).
[54] J. Erhardt, M. Iannetti, F. Dominguez, E. M. Hankiewicz, B. Trauzettel, G. Profeta, D. Di Sante, G. Sangiovanni, S. Moser, and R. Claessen, Backscattering in topological edge states despite time-reversal symmetry, Nature Communications **16**, 8209 (2025).
[55] J. Bardeen, Tunnelling from a many-particle point of view, Physical Review Letters **6**, 57 (1961).
[56] C. J. Chen, *Introduction to Scanning Tunneling Microscopy* (Oxford University Press, 1993).
[57] R. Wiesendanger, *Scanning Probe Microscopy and Spectroscopy: Methods and Applications* (Cambridge University Press, 1994).
[58] B. Voigtländer, *Scanning Probe Microscopy: Atomic Force Microscopy and Scanning Tunneling Microscopy* (Springer, Berlin, 2015).
[59] One might instead attribute the spin selectivity to a spin-dependent matrix element computed from the helical wavefunctions of the tip. Such an elastic matrix element, however, is independent of the bias voltage and cannot account for the experimentally observed sign reversal of the spin signal when the bias is reversed.
[60] T. E. Feuchtwang, Tunneling theory without the transfer-Hamiltonian formalism. I., Physical Review B **10**, 4121 (1974).
[61] W. Sacks and C. Noguera, Generalized expression for the tunneling current in scanning tunneling microscopy, Physical Review B **43**, 11612 (1991).
[62] D. Wortmann, H. Ishida, and S. Blügel, Embedded Green-function formulation of tunneling conductance: Bardeen versus Landauer approaches, Physical Review B **72**, 235113 (2005).
[63] C. Caroli, R. Combescot, P. Nozières, and D. Saint-James, Direct calculation of the tunneling current, Journal of Physics C: Solid State Physics **4**, 916 (1971).
[64] S. Datta, *Quantum Transport: Atom to Transistor* (Cambridge University Press, 2005).
[65] X. Sun, K.-Y. Zhang, S.-Z. Zhou, and H.-H. Fu, Robust chirality-induced spin selectivity in topologically chiral molecular knots, Nature Communications **17**, 1231 (2026).
[66] See Supplemental Material accompanying this manuscript for probe self-consistency equations, the spectrum, and edge-mode details.
[67] B. K. Nikolić and S. Souma, Decoherence of transported spin in multichannel spin-orbit-coupled spintronic devices: Scattering approach to spin-density matrix from the ballistic to the localized regime, Physical Review B **71**, 195328 (2005).
[68] S. Banerjee, A. Aishwarya, F. Liu, L. Jiao, V. Madhavan, E. J. Mele, and P. Coleman, Axionic tunneling from a topological kondo insulator, arXiv:2512.05057 (2025).
[69] M. Dzero and B. M. Andersen, Odd-parity surface magnetism in a kondo insulator, arXiv:2610.12573 (2026).
[70] M. Dzero and B. M. Andersen, Spin-polarized tunneling from a kondo insulator: equilibrium surface magnetism versus magneto-electric response in SmB_6, arXiv:2610.36886 (2026).
[71] H. Weng, X. Dai, and Z. Fang, Transition-metal pentatelluride ZrTe5 and HfTe5: A paradigm for large-gap quantum spin hall insulators, Physical Review X **4**, 011002 (2014).
[72] R.-Z. Liu, X. Huang, L.-X. Zhao, L.-M. Liu, J.-X. Yin, R. Wu, G.-F. Chen, Z.-Q. Wang, and S. H. Pan, Experimental observations indicating the topological nature of the edge states on HfTe5, Chinese Physics Letters **36**, 117301 (2019).
[73] R. Wu, J.-Z. Ma, S.-M. Nie, L.-X. Zhao, X. Huang, J.-X. Yin, *et al.*, Evidence for topological edge states in a large energy gap near the step edges on the surface of ZrTe5, Physical Review X **6**, 021017 (2016).

Supplementary Files

This is a list of supplementary files associated with this preprint. Click to download.

- Supplementary.pdf
- Supplementary.pdf